# Collisionless Magnetic Annihilation in Relativistic Laser-Plasma Interactions

Yanjun Gu[1], Ondrej Klimo[1,2], Deepak Kumar[1], Yue Liu[1], Sushil Singh[1], Sergei V. Bulanov[3], Timur Zh. Esirkepov[3], Stefan Weber[1], and Georg Korn[1]

[1]Institute of Physics of the ASCR, ELI-Beamlines project, Na Slovance 2, Prague 18221, Czech Republic;
[2]FNSPE, Czech Technical University in Prague, 11519 Prague, Czech Republic;
[3]Advanced Photon Research Center, Japan Atomic Energy Agency, 8-1-7 Umemidai, Kizugawa-shi, Kyoto 619-0215, Japan

## ABSTRACT

Magnetic reconnection is one of the fundamental phenomena in space and astrophysics. Through the rearrangement of magnetic field topology, it converts the magnetic energy to kinetic energy. Recently, ultra-high intensity laser pulses provide a new regime to generate and investigate magnetic reconnection with laser-plasma interactions. In this paper, we report a regime to induce collisionless magnetic annihilation by ultra-short laser pulses and plasmas. Two magnetic dipoles with amplitudes as high as giga-Gauss are propagating and expanding in the target . The magnetic field lines with opposite direction annihilate each other in the central plane and form a current sheet. The inductive longitudinal electric field grows in the current sheet and accelerates the electrons backwards. This regime may be beneficial for the potential experiments to be carried out on large laser facilities such as ELI.

**Keywords:** magnetic reconnection, magnetic vortex, laser-plasma interaction

## 1. INTRODUCTION

The process of magnetic reconnection is always accompanied with the formation of a current sheet, where the magnetic field lines with opposite directions annihilate each other. Therefore, the research on magnetic annihilation and the corresponding energy dissipation becomes important. Early works, such as famous Sweet-Parker model,[1] based on resistive magnetohydrodynamics (MHD) theory regard Ohmic dissipation as the main energy conversion mechanism. However, the predicted reconnection rates are too slow to explain the observations in universe. This suggests that many magnetic reconnections actually occur in collisionless plasmas such as solar corona. The corresponding theoretical and experimental investigations have been reviewed in many papers.[2–5]

Recently, with the development of laser facilities, TW ($10^{12}$W) and PW ($10^{15}$W) pulses are available which allows to investigate magnetic reconnection in laboratory by the new method of laser-plasma interactions. Pioneering experiments were made by Nilson *et al.*[6] and Li *et al.*[7] using long pulses (1ns) and solid targets. J. Y. Zhong *et al.*[8] obtained X-ray source by reconnection outflows with nanosecond pulses and solid Aluminum targets. In all the above experiments, the magnetic fields are created by the hot electrons, which are accelerated by the laser ponderomotive force. The magnetic field lines flow and expand with the electrons and the time scales for reconnection are from ps ($10^{-12}$s) to ns $10^{-9}$s. Except the experiments, PIC (Particle-in-cell) kinetic simulations and MHD simulations provide researches in explaining the mechanisms of magnetic reconnections.[9–11]

In this proceeding, we report a fast collisionless magnetic annihilation in relativistic laser-plasma interactions by 2.5-dimensional PIC simulations. The relativistic electromagnetic code 'EPOCH' is used in the simulations.[12] The schematic of the simulation is shown in Figure 1. A fully ionized hydrogen plasma locates in 20 ($\lambda$) $< x <$ 122 ($\lambda$) and $-20$ ($\lambda$) $< y <$ 20 ($\lambda$). In transverse direction, the density distribution of the target is uniform. In longitudinal direction, the density increases linearly from 0 to 0.1 $n_c$ in 20 ($\lambda$) $< x <$ 22 ($\lambda$) and remains constant for 22 ($\lambda$) $< x <$ 62 ($\lambda$), where $n_c = \frac{m_e\omega^2}{4\pi e^2}$ is the plasma critical density, $m_e$, $\omega$ and e represent the electron mass, laser angular frequency and electric charge, respectively. The long downramp region is in 62 ($\lambda$) $< x <$ 122 ($\lambda$), where the density linearly decreases to 0. Two s-polarized Gaussian pulses with the peak

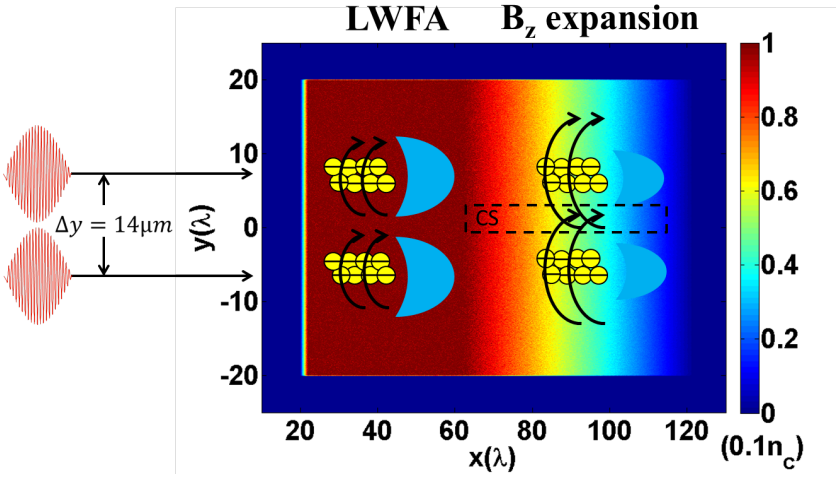


Figure 1. (color online) Schematic of the simulation model.

intensity of $10^{21}$W/cm$^2$ propagate along longitudinal direction are focused on the target left boundary. The separation between two pulses are 14 $\lambda$ as shown in Fig. 1, i.e. the optical axes of two pulses are $\pm 7$ $\lambda$. Different from the experiments and simulations described above, the pulses in our simulations are ultra-short with the pulse duration $\tau = 15$ $fs$. The lasers spot sizes is 3 $\lambda$ and the laser wavelength is $\lambda = 1$ $\mu m$. Free boundary conditions are employed and the initial plasma temperature is 0K.

The whole process can be divided in two stages. In the first stage, two electron beams are formed by the LWFA (laser wakefield acceleration) effect. The corresponding magnetic dipole structures are produced by the electron beams according to Ampere's law. Both the energy of electron beam and the strength of the magnetic field are growing in the density plateau region in this stage. In the second stage, the magnetic fields expand in transverse direction after they enter the downramp region. The magnetic fields with opposite direction annihilate in the current sheet. During the annihilation, it is the displacement current which balances the variation of the magnetic field. A strong inductive electric field is generated in the current sheet which intensively accelerates charged particles. In our simulations, we find the high energy electrons accelerated in backward by this field in the current sheet.

## 2. ELECTRON BEAM ACCELERATION AND MAGNETIC FIELD GENERATION

In this part, we discuss the electron acceleration and the corresponding magnetic fields generation in the first stage. It is well known that short laser pulse generate strong wakefield when it is propagating in a plasma. The strength of this longitudinal electric field is given by[13]

$$E_{max} = 0.38(2\gamma)(1+\gamma)^{(-1/2)}\sqrt{(n_0)} \approx 34 \text{ GV/cm}. \quad (1)$$

Here $\gamma$ is the relativistic factor of the electrons, which is approximately equal to the dimensionless amplitude of laser pulse $a_0 = eE_0/m_e\omega c$. The electron density distribution at 51 $T_0$ is plotted in Fig. 2(a). Two bubble structures have formed and two electron beams are trapped by each bubble. The electrons are accelerated by the longitudinal wakefield to several tens MeV inside the bubble. Fig. 2(b) presents the electron momentum distribution along y-direction (i.e. $y - p_x$). The electron highest energy reaches about 50 $MeV$ at this moment. The return electrons with maximum momentum locate along the laser pulse. However, between the two pulses (i.e. $-\lambda < y < \lambda$), the electrons momentum is rather small. The distribution of backward accelerated electrons is an important point to distinguish the outflow in magnetic annihilation which will be presented below.

According to the Ampere circuital law, electron current generates magnetic loop surrounding it. In Fig. 2(c), two symmetric magnetic dipoles are produced by the LWFA electron beams. The amplitude of the magnetic fields can be estimated by Ampere-Maxwell law as

$$c\nabla \times B = 4\pi J + \partial E/\partial t. \quad (2)$$

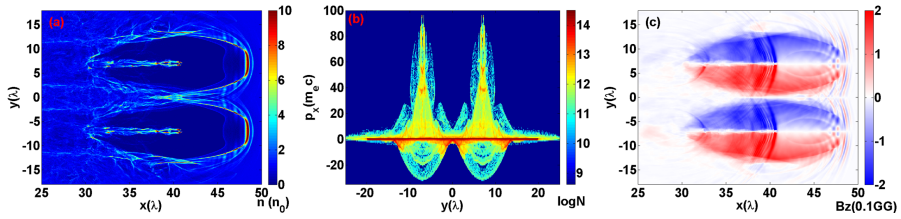


Figure 2. (color online) At 51 $T_0$, (a) The electron density distribution. (b) Electron momentum $y - p_x$ distribution. (c) The $B_z$ distribution.

Assuming the quasi electrostatic condition as $\partial_t E = 0$ and the maximum radius of the dipole is $R \approx c\sqrt{a_0}/\omega_p$. It gives the amplitude of magnetic field $B_z = 4\pi n_0 ec\sqrt{\gamma}/\omega_p \approx 0.2GG$.[14] At this stage, the two magnetic dipoles are separate. One can find the amplitude of $B_z$ in the simulation is well agree with the theory estimation.

## 3. MAGNETIC EXPANSION, ANNIHILATION AND PARTICLE ACCELERATION

After entering the density downramp, the magnetic dipoles begin expanding in the transverse direction. It is because the force acting on the bubbles which is proportional to $\nabla n \times \Omega$, where $\Omega$ is the potential vorticity.[15] In the center region, there is no enough space for the dipoles to expand freely. The magnetic fields with opposite directions attach each other and start the process of annihilation. Fig. 3(a) is the magnetic field distribution at 141 $T_0$, the dipole structures are asymmetric with large size of the outer part and small size of the inner part. In 105 $\lambda < x <$ 115 $\lambda$, the inner magnetic fields have been completely annihilated. At the same time, the annihilation of magnetic fields accompany with the growth of longitudinal electric field in the annihilation region, which is one of the signatures of magnetic annihilation. The layer where magnetic fields annihilate and electric fields grow is also called current sheet. In Fig. 3(b), we compare the profile of $E_x$ along laser axis and current sheet at 141 $T_0$. One can find in the region where magnetic fields cancelled each other, (i.e. 105 $\lambda < x <$ 115 $\lambda$), there is a strong longitudinal electric field in the current sheet, which is even higher than the field along laser axis. The growth of electric field indicates energy conversion between magnetic field and electric field.

To explain the generation of the inductive electric field, we plot the contributions of each term in Ampere-Maxwell law (Eq. (2)) in Fig. 3(c). All the curves are spatial averaged over the current sheet ($-\lambda < y < \lambda$). In the region of annihilation, the electron density is very low due to the downramp distribution, therefore the corresponding electron current is also small. In this case, the variation of the magnetic field, $< c\nabla \times B/4\pi >_z$, cannot be fully compensated by the electron current. The growth of the displacement current, $J_D = \partial E/\partial t$, is necessary to balance the equation and the corresponding electric field is induced. A strong outflow particles is another signature in magnetic annihilation. Due to the growth of the inductive electric field, a bunch of high energy electrons ejects backwards in the current sheet is expected. In Fig. 3(d), the distribution of momentum shows the acceleration effect in the current sheet and the maximum momentum reaches 100 $m_e c$. Compared with the distribution in Fig. 2(b), we find the particles in current sheet get more energy than the particles along laser axis after magnetic annihilation occurs. This proves the magnetic field release its energy to particles in annihilation process via the displacement current and inductive electric field.

## 4. CONCLUSIONS

In this proceeding, a fast magnetic annihilation is obtained with two ultra-short PW laser pulses and non-uniform underdense plasma. Strong inductive electric field and high energy outflow particles are detected. The displacement current plays an important role in magnetic annihilation, which balances the variation of magnetic fields and induces the inductive electric field. The results are beneficial for the potential experiments in the large laser facilities such as ELI project.[16]

## ACKNOWLEDGMENTS

This work was supported by the ELI (Project No. CZ.1.05/1.1.00/02.0061). Computational resources were provided by the MetaCentrum under the program LM2010005 and by IT4Innovations Centre of Excellence

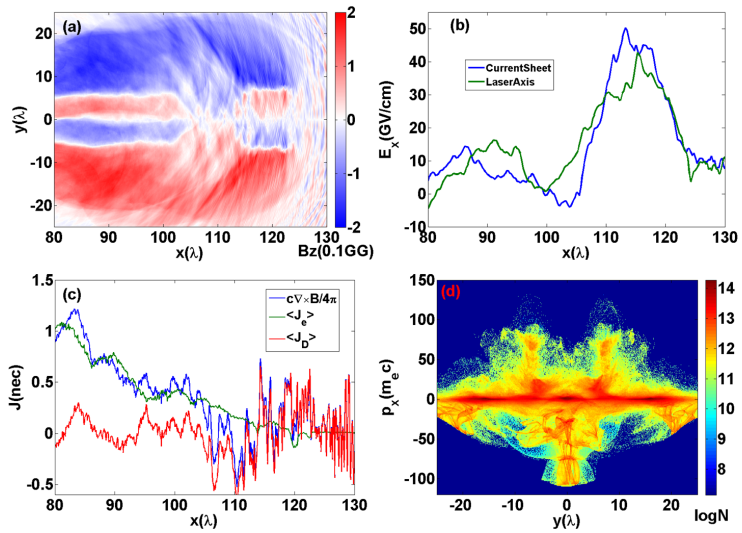


Figure 3. (color online) At 141 $T_0$, (a) The magnetic field distribution. (b) The longitudinal electric field profile along current ($y = 0$) and laser axis ($y = 7\ \lambda$). (c) The contributions of terms in Maxwell-Ampere equation. (d) Electron momentum $y - p_x$ distribution.

under projects CZ.1.05/1.1.00/02.0070 and LM2011033. The EPOCH code was developed as part of the UK EPSRC funded projects EP/G054940/1.

## REFERENCES

1. E. N. Parker *J. Geophys. Res.* **62**, pp. 509–520, 1957.
2. D. Biskamp *Phys. Fluids* **29**, pp. 1520–1531, 1986.
3. J. F. Drake, R. G. Kleva, and M. E. Mandt *Phys. Rev. Lett.* **73**, pp. 1251–1254, 1994.
4. S. V. Bulanov, T. Z. Esirkepov, D. Habs, F. Pegoraro, and T. Tajima *Eur. Phys. J. D* **55**, pp. 483–507, 2009.
5. S. V. Bulanov, T. Z. Esirkepov, M. Kando, J. Koga, K. Kondo, and G. Korn *Plasma Phys. Rep.* **41**, pp. 1–51, 2015.
6. P. M. Nilson, L. Willingale, M. C. Kaluza, C. Kamperidis, S. Minardi, M. S. Wei, P. Fernandes, M. Notley, S. Bandyopadhyay, M. Sherlock, R. J. Kingham, M. Tatarakis, Z. Najmudin, W. Rozmus, R. G. Evans, M. G. Haines, A. E. Dangor, and K. Krushelnick *Phys. Rev. Lett.* **97**, p. 255001, 2006.
7. C. K. Li, F. H. Sguin, J. A. Frenje, J. R. Rygg, R. D. Petrasso, R. P. J. Town, O. L. Landen, J. P. Knauer, and V. A. Smalyuk *Phys. Rev. Lett.* **99**, p. 055001, 2007.
8. J. Zhong, Y. Li, X. Wang, J. Wang, Q. Dong, C. Xiao, S. Wang, X. Liu, L. Zhang, L. An, F. Wang, J. Zhu, Y. Gu, X. He, G. Zhao, and J. Zhang *Nat. Phys.* **6**, pp. 984–987, 2010.
9. M. Hoshino, T. Mukai, T. Terasawa, and I. Shinohara *J. Geophys. Res. Space Physics* **106**, pp. 25979–25997, 2001.
10. Y. L. Ping, J. Y. Zhong, Z. M. Sheng, X. G. Wang, B. Liu, Y. T. Li, X. Q. Yan, X. T. He, J. Zhang, and G. Zhao *Phys. Rev. E* **89**, p. 031101, 2014.
11. J. F. Drake, D. Biskamp, and A. Zeiler *Geophys. Res. Lett.* **24**, pp. 2921–2924, 1997.
12. C. P. Ridgers, J. G. Kirk, R. Duclous, T. G. Blackburn, C. S. Brady, K. Bennett, T. D. Arber, and A. R. Bell *J. Comput. Phys.* **260**, pp. 273–285, 2014.
13. P. Sprangle, E. Esarey, A. Ting, and G. Joyce *Appl. Phys. Lett.* **53**, pp. 2146–2148, 1988.
14. G. A. Askaran, S. V. Bulanov, F. Pegoraro, and A. M. Pukhov *JETP Lett.* **60**, p. 251, 1994.
15. J. Nycander and M. B. Isichenko *Phys. Fluids B* **2**, pp. 2042–2047, 1990.
16. G. Mourou, G. Korn, W. Sandner, and J. Collier *CNRS, Paris* , 2011.